A mechanism of strain hardening and Bauschinger effect: shear-history-dependent microstructure of elasto-plastic suspensions

Stéphanie Deboeuf, Lucie Ducloué, Nicolas Lenoir, Guillaume Ovarlez

A mechanism of strain hardening and Bauschinger effect: shear-history-dependent microstructure of elasto-plastic suspensions

Stéphanie Deboeuf
*Sorbonne Université, CNRS, UMR 7190, Institut Jean Le Rond d'Alembert, 75005 Paris, France.**

Lucie Ducloué
Laboratoire Navier, Univ. Gustave Eiffel, ENPC, CNRS, F-77447 Marne-la-Vallée, France

Nicolas Lenoir
Univ. Grenoble Alpes, Grenoble INP, CNRS, 3SR, F-38000 Grenoble, France.

Guillaume Ovarlez
Univ. Bordeaux, CNRS, Solvay, LOF, UMR 5258, F-33608 Pessac, France
(Dated: June 23, 2022)

Dispersing solid hard particles in an elasto-plastic material leads to important shear-history dependence of the behavior, namely strain hardening and Bauschinger effect. Strain hardening is observed as the progressive strengthening of a material during its plastic deformation and is usually associated with ductility, a property often sought after in composite materials to postpone fractures and failure. In addition, anisotropic mechanical properties are developed, the material resistance being larger in the direction of the imposed flow, which is referred to as the Bauschinger effect. We show that this is related here to shear-history-dependent particle-pair distribution functions. Roughness and interparticle contacts likely play a major role, as replacing hard particles by non-deformable bubbles modifies the suspension microstructure and suppresses strain hardening. Beyond suspensions, our study provides new insight in the understanding and control of strain hardening and Bauschinger effect in composite materials.

I. INTRODUCTION

A. From suspensions to composite materials

Polymers including elastomers, commonly called plastics and rubbers, are standard materials in the manufacturing industry. To improve their mechanical properties, solid inclusions such as particles or fibers are often embedded in the polymer matrix [1, 2]. They then form composites, with a microstructure emerging at the inclusion scale.

These materials are usually processed in their molten state (in moulding, coating, three dimensional printing...), in which they are handled as suspensions of solid particles in a fluid. This molten state offers the opportunity to tune the final microstructure as a function of flow history (*e.g.*, by forcing the fiber alignment in the casting direction for fibrous materials [3]).

As for any architectured material, such composites may reach optimal mechanical properties for specific microstructures only. Materials with high strength and ductility are particularly sought after for postponing fractures and failure [4, 5]. Appropriate preparation in the molten state is *a priori* needed to tune the microstructure and thus the solid state properties [2].

Strain hardening (also named work hardening) is a mechanism governing the strength and the ductility of materials, as it leads to higher resistance and higher rupture strain in some specific directions. Strain hardening is observed as the progressive strengthening of a material – increase of its yield stress – during its plastic deformation [6].

In order to study the emergence of strain hardening in composite materials and the impact of flow history on it, a suspending yield-stress fluid can be used as a model material. Indeed, it has both the characteristics of a fluid, when stresses are larger than its yield stress, thus being relevant to model the molten composite, and those of a solid otherwise, then being relevant to model the solid composite. Large strains experienced by yield-stress suspensions can be of the same order as typical strains of some polymeric composites (elastomers, rubbers) enhancing their relevance as model systems. Before presenting our study on such elasto-plastic suspensions, we discuss below the main characteristics of strain hardening in solid materials and yield-stress fluids. We then review some features of the coupling between flow and microstructure in suspensions.

B. Elasto-plasticity and strain hardening

Plasticity is at the crossroad of solid and fluid behaviors. In solid mechanics, plasticity is defined as the emergence of irreversible deformations; it is thus a flow, which is the focus of fluid mechanics. There is a critical stress, the yield stress σ_Y, below which only reversible deformations (defining elasticity) are found and above which plas-

* sdeboeuf@dalembert.upmc.fr

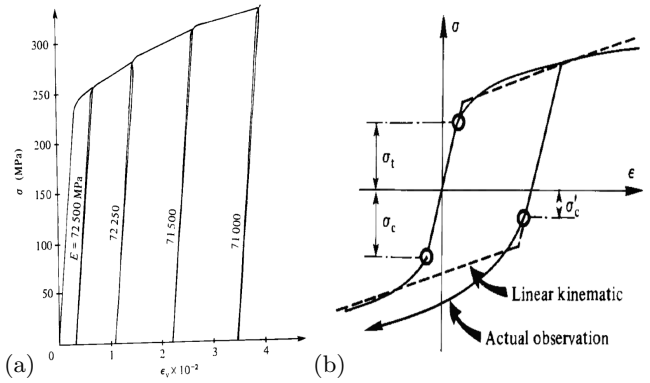

FIG. 1. From Lemaitre and Chaboche [6], a classical book on solid materials. (a) Strain-hardening curves with unloading-reloading steps for a solid (elasto-plastic) metal using quasi-static shear-rate-controlled flow. After a given loading, unloading the material allows to disentangle reversible and irreversible deformations, whereas reloading it allows to measure its yield stress in its current state and to evidence its progressive strengthening. (b) Typical stress-strain response to a cycle of quasi-static traction and compression. Starting from a non-plastified initial state, the yield stress measured in both traction and compression is the same ($\sigma_t = \sigma_c$), whereas it is smaller when measured in compression after an initial plastic traction flow (σ_c'). This influence of the plastic flow on the anisotropy of the mechanical properties is due to strain hardening (Bauschinger effect).

tic flows take place. Reversible and irreversible deformations can be disentangled by loading (up to a given stress $\sigma \neq 0$) and subsequently unloading a material (back to rest, defined by a zero stress), as shown by the typical stress-strain response of a solid metal in Fig. 1a. When the shear stress σ is below the yield stress σ_Y of the material in its initial (reference) state, the strain goes back to 0 when the material is unloaded. When it is higher than σ_Y, the unloading path is different from the loading path and the final accumulated (plastic) deformation is $\neq 0$.

In addition, strain hardening is commonly observed [Fig. 1(a)]. After loading the material up to a stress $\sigma = \sigma_0 > \sigma_Y$ for which plastic flow occurs, the unloading step and its subsequent reloading step are superposed, showing that the material can now be loaded reversibly until $\sigma = \sigma_0$, which is thus the current material yield stress (*i.e.*, in its current reference state). Reloading the material with a higher value of σ then leads to additional plastic flow and to further increase of the yield stress. The response to a systematic succession of loading and unloading steps highlights the progressive increase of the yield stress with the plastic flow.

Strain hardening can lead to anisotropic mechanical properties, with a smaller yield stress in directions different to that of the previously imposed plastic flow [6]. This is illustrated during a cycle of quasi-static traction and compression in Fig. 1b: after a plastic flow in traction (σ, $\epsilon > 0$), the yield stress σ_c' measured in compression has a smaller value than the yield stress σ_t achieved in traction; by contrast, for a non-plastified initial state, the yield stress is independent of the loading direction, σ_t and σ_c measured, respectively, in traction and compression being equal. This anisotropy is not intrinsic but is induced by a dependence of the mechanical properties on the load history (its amplitude and/or its direction); this phenomenon is called the Bauschinger effect.

Strain hardening is ubiquitous in solid materials: it is found in metals and alloys [7] (crystals [8], nanostructured metals [9], metallic glasses [10]), polymer glasses [11, 12], composite materials [13], polymer gels [14, 15], magnetorheological gels [16], colloidal gels [17], and soft-glassy materials [18–21]. In crystalline solids, reversible movements of atoms, thus elasticity, cease when crystalline defaults (dislocations) appear and move irreversibly, which is responsible for plasticity. After a given plastic strain, the interaction with other pre-existing defaults might prevent further displacement of these defaults, which leads to an increase of the yield stress in a proposed mechanism of strain hardening [22–24]. Despite the absence of long-range order and thus of dislocations, amorphous compounds such as metallic glasses can also exhibit hardening [10]: the interplay between shear and the density of microstructural units (called shear-transformation zones) is here at play [25].

In complex fluids, plasticity is observed in soft-glassy materials (concentrated emulsions, foams, microgel suspensions, colloidal glasses...), also referred to as yield-stress fluids. The focus has been for long on visco-plasticity: their elasto-plastic behavior – especially relevant for quasi-static flows at small shear rates – has been largely disregarded. The elasto-plastic behavior of yield-stress fluids has first been modeled as a perfect elasto-plastic behavior [26]. However, when studied in detail, it is observed that strain hardening occurs as well in these materials. Recently, kinematic hardening was shown to be relevant [19] and incorporated into continuum modelling of the elasto-visco-plastic response of yield-stress fluids [21]. As many elasto-plastic fluids can deform indefinitely without experiencing any rupture – contrary to elasto-plastic solids – they can experience successive strain-hardening histories in different directions, which makes them convenient model materials to study in detail this phenomenon.

C. Suspension microstructure coupled to rheology

In suspensions, a microstructure emerges at the scale of the suspended inclusions, which can then be considered as the relevant 'micro' scale [27–29]. This microstructure can exhibit an anisotropy, observed not only with elongated inclusions but also with spherical rigid inclusions in the form of a spatial distribution anisotropy. It finds its origin in the fore-aft asymmetry of particle pair trajectories induced by direct interparticle contacts [27, 30]. This effect, observed in Newtonian fluids, is amplified for non-

linear suspending materials such as plastic fluids [31, 32]. Moreover, this microstructure depends on the flow history [29, 33]. As the microstructure is coupled to the macroscopic properties, the mechanical response should then be affected by different flow histories and different initial conditions [33, 34].

To investigate the possible role of microstructure in the mechanical properties of elasto-plastic materials and evidence a mechanism of strain hardening, we use model suspensions of spherical inclusions in yield-stress fluids. These inclusions are both solid spheres and non-deformable bubbles, in order to highlight the role of solid contacts. On one hand, we characterize their microstructure; on the other hand, we study their mechanical properties in the framework of elasticity, plasticity and strain hardening. In particular, we apply different types of loading (rotational shear, squeeze) to our samples and we study their response to shear reversal to investigate the Bauschinger effect and the dependence of the microstructural and macroscopic properties on the load history.

In part II, we present the materials and the experimental methods allowing us to do both macroscopic rheology and microstructure characterization thanks to three-dimensional imaging, which results are presented respectively in parts III and IV. The results, obtained on both suspensions of solid spheres and of non-deformable bubbles in yield-stress fluids, are compared and discussed in part V.

II. MATERIALS AND METHODS

We study elasto-visco-plastic suspensions (Sec. II A) as model composite materials. Different rheometric methods (Sec. II B) are used to prepare materials with various strain histories and to characterize their elasto-plastic response, in particular the evolution of the elastic modulus and of the yield stress during their hardening. In parallel, we characterize their microstructure with the methods exposed in Sec. II C for the same shear histories.

A. Materials

Two types of suspensions are studied here: solid particles or non-deformable bubbles suspended in an elasto-visco-plastic fluid. Fluids and particles of different properties, reported in Table I, are used. Their composition is chosen in particular to guarantee their suitability to the different methods used below – rheometry or X-ray micro-tomography.

Elasto-visco-plastic fluids are concentrated emulsions. A direct emulsion (i) is prepared by dispersing silicone oil (V350) at a volume fraction 70% in a 36 wt%/64 wt% mixture of water/glycerol, in which surfactant TTAB has been added at 3% in mass. An inverse emulsion (ii) is prepared by dispersing a water solution of iodine sodium (15 wt%) at a volume fraction 77.5% in dodecane oil containing surfactant SPAN80 (7.5 wt%) – iodine sodium is used in the dispersed phase to stabilize the emulsion and enhance contrast for X-ray imaging.

Air bubbles have a mean diameter $d = 100$ μm (0) or $d = 280$ μm (1) and solid particles are polystyrene (PS) spheres of mean diameter $d = 80$ μm (2) or $d = 140$ μm (3). With such sizes, particles and bubbles are non-Brownian. Bubbles are used here as analogues of frictionless and perfectly smooth rigid particles [35]; this analogy is valid as long as the bubbles remain undeformed by the flow. As shown by Ducloué *et al.* [36], bubbles of diameter d in a fluid of yield stress τ_Y^∞ remain undeformed at the onset of flow as long as the plastic capillary number $Ca_{plast} = \tau_Y^\infty/(4\Gamma/d) \lesssim 0.1$, where Γ is the yield-stress fluid surface tension (here, that of the emulsion continuous phase (i), for which $\Gamma = 35$ mN.m^{-1}, $\tau_Y^\infty = 20$ Pa) and $d = 100$ μm (0) or $d = 280$ μm (1). In our experiments, $Ca_{plast} \simeq 0.01$ (0) or $\simeq 0.04$ (1): bubbles remain spherical. The bubbly suspensions are prepared as described in Ducloué *et al.* [36].

In the following, suspensions (0,1) and (2) consist, respectively, in air bubbles (0,1) and solid inclusions (2) in the elasto-plastic fluid (i), whereas suspensions (3) have solid inclusions (3) in the elasto-plastic fluid (ii).

Air (0) and solid (2,3) inclusions are approximately monodisperse (their diameter standard deviation is smaller than 20% of their mean diameter), whereas bubbles (1) are poyldisperse (their diameter standard deviation is half of their mean diameter). Indeed, bubble suspensions (1) consist of suspensions (0) prepared $\sim$1 h before the experiments, due to incompressible delay times before imaging, so that these bubbles have aged since their preparation: their mean diameter has increased by a factor 2.8 and their diameter distribution has widened (see Fig. 15 in Appendix A); this coarsening is a classical feature of foams [37]. Special attention has been paid to the analysis of their microstructure to take into account their polydispersity (Sec. II C).

TABLE I. Properties of the elasto-visco-plastic fluids, air bubbles and solid particles: density ρ_f, elastic shear modulus G'^∞ and yield stress τ_Y^∞ for the elasto-plastic properties, index n and consistency k for the viscous properties of the suspending fluid; density ρ and average diameter d of the particles or bubbles, volume fraction ϕ of the bubbles or particles in the specified suspending fluid.

Elasto-visco-plastic fluid					
Sample	ρ_f	G'^∞ (Pa)	τ_Y^∞ (Pa)	n	k (Pa.s^n)
(i)	1.01	650	20	0.45	0.9
(ii)	1.05	350	24.5	0.5	5

Bubbles/Solid particles in suspension					
Sample	Fluid	Inclusions	ρ	d (μm)	ϕ
(0)	(i)	Air	0.00	100 ± 20	$0 - 50\%$
(1)	(i)	Air	0.00	280 ± 140	$30, 37.5\%$
(2)	(i)	PS	1.05	80 ± 5	$0 - 50\%$
(3)	(ii)	PS	1.05	140 ± 10	$0, 35, 40\%$

The droplet size of both concentrated emulsions is of the order of 1 μm, much smaller than the particle and the bubble size. This ensures that the emulsion is seen as a continuous material – an elasto-visco-plastic fluid – by the particles [33, 38, 39]. Solid PS particles and suspending fluids, of density ρ and ρ_f respectively, are approximately density-matched to avoid any buoyancy effects, whereas air bubbles are much lighter than the suspending fluid. However, the solid fraction ϕ of all suspensions is observed to remain uniform within our rheological set-ups (thanks to X-ray imaging [29]), consistent with the long timescale that can be computed for significant shear-induced sedimentation or shear-induced creaming within our experimental conditions [40–42].

The steady-state visco-plastic behavior of our fluids is well described by a Herschel-Bulkley law $\tau = \tau_Y^\infty + k\dot{\gamma}^n$, while their steady elasto-plastic behavior is accounted for by their elastic shear modulus G'^∞ and their yield stress τ_Y^∞. In the following, we disregard viscous effects as the Bingham number $Bi = \tau_Y^\infty/(k\dot{\gamma}^n)$ is large in the experiments: $Bi \simeq 150$ and $Bi \simeq 50$ for fluids (i) and (ii) respectively. We focus on the elasto-plastic behavior of the suspensions and on the impact of shear history on this behavior.

B. Macroscopic rheology

Our rheological set-ups are parallel plates geometries (Fig. 2) of diameter D and gap H, controlled by a Kinexus rheometer from Malvern (now Netzsch). The plates of the shear cell are serrated to prevent slippage of the suspension at the solid boundaries. The top plate is rotated at a rate Ω while keeping fixed the bottom plate, leading to a simple shear of the fluid in the azimuthal plane (θz), the single non-zero value of the shear rate tensor being:

$$\dot{\gamma}(r) = 2d_{z\theta}(r) = \Omega r/H, \tag{1}$$

with an azimuthal velocity $u_\theta(r,z) = \Omega z r/H$, (r,θ,z) being the cylindrical coordinates [43]. The rotational shear is not homogeneous but depends linearly on the radial direction r. As a convenient estimate of the overall shear rate, we use here: $\dot{\gamma} = 3\Omega D/(8H)$. In the same parallel plates geometry, a squeeze flow can be imposed by translating vertically one plate at a velocity V. It can be approximated by a simple shear flow in the radial plane (rz), in the case of a large aspect ratio D/H and of no slip at the solid boundaries [40, 43, 44]. In this case, the shear rate $\dot{\gamma}_\perp(r,z) = 2d_{zr}(r,z)$ is inhomogeneous and *a priori* unknown: it depends on the rheology of the fluid of interest. As a convenient estimate of the overall squeeze shear rate, we then use [40] $\dot{\gamma}_\perp = 3VD/(2H^2)$.

These two simple shear flows are orthogonal, meaning that their respective velocity gradient-velocity planes are perpendicular to each other [40, 45]. In order to shear the material in the parallel plates geometry, it is first poured on the bottom plate, then it is squeezed by the top plate to reach the required gap. So even if the interest is in a rotational shear, the material always experiences first a squeeze flow during its loading in the geometry, which sets its initial state. That is why studying the response of a material without any pre-shear is not strictly achievable with our set-ups.

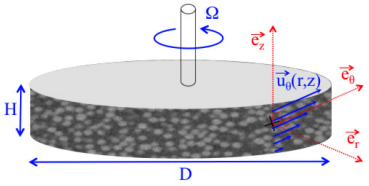

FIG. 2. Scheme of a rotational shear flow in a parallel plates set-up used for rheometry: the suspension velocity $u_\theta(r,z)$ is aligned with the azimuthal direction, Ω is the rotational velocity of the top plate, D and H are the plates diameter and gap. (r,θ,z) are the cylindrical coordinates.

1. *Probing the elasto-plastic response*

A standard rheological test to measure a material yield stress and to study its elasto-plastic response consists in imposing a quasi-static plastic shear flow [46]. Two types of tests are performed.

Shear-rate-controlled test. A small constant shear rate $\dot{\gamma} = 10^{-2}$ s^{-1} is imposed until a steady stress – the yield stress τ_Y^∞ – is observed ('small' shear rate means that viscous effects can be neglected, which is quantified by the Bingham number Bi).

Shear-stress-controlled test. Constant stresses $\tau_n = n\Delta\tau$ are applied, varied by 20 steps of $\Delta\tau = \tau_Y^\infty/20$ (each step being applied for 10s) until the yield stress τ_Y^∞ is reached; the final step is imposed for a strain $\gamma \sim 3$, sufficient to reach a steady flow (at a shear rate $\simeq 10^{-2}$ s^{-1}). Only the last step leads to a steady plastic flow; the other steps are characterized by a transient plastic flow, with a vanishing shear rate, as classically observed below the yield stress in yield-stress fluids [46].
The interest of this procedure (see Sec. II B 3) is to measure continuously the elastic modulus evolution with the help of parallel superposition, which can be used only in controlled-stress mode with our rheometer. Prior determination of the yield stress τ_Y^∞ in a shear-rate-controlled test is necessary to set-up this stress-controlled test.

2. *Shear histories*

Such quasi-static shear flows are imposed in a direction – called reference direction – to suspensions that have been pre-sheared in various directions, which orientations are described relatively to the reference direction. This allows us to investigate the dependence of the elasto-plastic behavior on shear history.

Specifically, we focus on three cases. When the material is pre-sheared in the same direction as that of the quasi-static plastic flow (at the same shear rate $\dot{\gamma} = 10^{-2}$ s^{-1}), it is denoted as 'pre-shear +' (or indicated by the exponent $^{+}$). When it is pre-sheared in the opposite direction, it is denoted as 'pre-shear −' (exponent $^{-}$). When it is pre-sheared in an orthogonal direction, it is denoted as 'pre-shear ⊥' (exponent $^{\perp}$).

In practice, the quasi-static shear flow is obtained by rotating the upper plate of the parallel plates geometry in a given direction. The experiment with pre-shear − is obtained by first rotating the plate in the opposite direction: it corresponds to a shear reversal [34] and to an initial condition that is the furthest from the steady plastic state. The experiment with pre-shear ⊥ is obtained by squeezing the material between the plates [40, 45] before rotating the upper plate.

3. *Disentangling elasticity and plasticity*

Unload-reload cycles (as in Sec. I B) and shear oscillations are used to measure both the current yield stress $\tau_Y(\gamma_p)$ and the current elastic shear modulus $G'(\gamma_p)$ of the suspensions throughout their shear histories, for different initial conditions. These current mechanical properties refer to the values measured on a given material state (the 'current state') after a controlled plastic deformation γ_p has been accumulated since the initial state. By contrast, the steady values τ_Y^{∞} and G'^{∞} are measured when the steady plastic flow is achieved ($\gamma_p \to \infty$).

Unload-reload cycles. In a shear-rate-controlled test beginning from $\gamma = 0$, the flow is stopped ($\dot{\gamma} = 0$ s^{-1}) after a given deformation, the stress is reduced to 0 Pa – corresponding to an unload step back to rest – the plastic deformation γ_p accumulated since the initial condition is recorded, and then the quasi-static plastic flow is started again ($\dot{\gamma} = 10^{-2}$ s^{-1}) – corresponding to a reload step – and this goes on for different values of the plastic deformation γ_p. This is similar to the method illustrated in Fig. 1a. The current yield stress $\tau_Y(\gamma_p)$ is measured as the stress threshold between reversible and irreversible responses of the suspension during a load-unload-reload cycle [6] for each plastic deformation γ_p.
In a shear-stress-controlled test, we emphasize that once plastic flow has stopped at a given τ_n value, the material can be unloaded/loaded reversibly from τ_n to 0, whereas an additional plastic flow takes place for any $\tau > \tau_n$; τ_n is thus the current material yield stress associated with the plastic deformation $\gamma_p(\tau_n)$.

Elastic modulus. In shear-rate-controlled tests, for each unload/reload cycle, when $\dot{\gamma}$ and τ are zero just before reload, the current elastic modulus $G'(\gamma_p)$ is measured thanks to small amplitude shear oscillations applied at high frequency ($f = 10$ Hz) and low stress amplitude ($\delta\sigma = 0.2$ Pa), in the linear regime.
In shear-stress-controlled tests, at each step τ_n, the strain increase $\gamma(t)$ is recorded in time as plasticity slowly develops. The elastic modulus $G'(\gamma)$ can then be measured continuously as a function of γ thanks to parallel superposition, that is small amplitude shear oscillations ($f = 10$ Hz, $\delta\sigma = 0.2$ Pa) superimposed to all stress imposed steps τ_n. As will be shown in Sec. III, the plastic strain is much larger than the elastic strain for the experiments of interest (shear reversal): the strain γ can thus be identified with the plastic deformation γ_p accumulated since the initial condition, and $G'(\gamma)$ is thus $G'(\gamma_p)$. The main interest of this experiment is thus to provide $G'(\gamma_p)$ throughout hardening with a much finer resolution on γ_p than in shear-rate-controlled tests. Note however that for each value of γ_p, $G'(\tau = 0)$ is measured at rest in the shear-rate-controlled tests, whereas $G'(\tau = \tau_n)$ is measured on the stressed material in the shear-stress-controlled tests; there might then be some differences between the measured values due to possible nonlinear elasticity.

C. Microstructure characterization

1. *X-ray imaging*

We have used the X-ray micro-tomography device located in Laboratoire Navier (described in detail in [29]), made up of an Ultratom scanner designed and assembled by RX Solutions (Annecy, France). Using the commercial software Xact, based on the filtered retroprojection algorithm adapted to cone-beam geometry [47], 3D images encoding for the X-ray absorption field are reconstructed from the recorded 2D radiographs (Fig. 3). Consistently with the definition of the final 3D images, 1440 radiographs have been recorded over 360°. Note that for each rotation angle, 6 radiographs (with an exposure time for one radiograph of 1/3 s) have been averaged to improve the signal to noise ratio. The final 3D images have a resolution of 12 μm and a definition of 1840x1840x170 voxels.

Before X-ray imaging, the suspension is sheared in a parallel plates geometry of diameter $D = 2$ cm and gap $H = 2$ mm (Fig. 2). We built a dedicated geometry [29] made of PMMA to ensure a low X-ray absorption by the set-up. This set-up can be used in the rheometer for shearing the material and characterizing its rheological response. After a given shear history in the rheometer, it can then be blocked thanks to a chuck, removed from the rheometer and carefully moved to the X-ray set-up, where it is put on the rotating stage for imaging. During the whole duration of imaging, the parallel plates set-up is blocked. We checked that these *ex-situ* experiments lead to the same results as *in-situ* ones [29]. More details can be found in Deboeuf *et al.* [29].

Special attention has been paid to reduce the delay to a few minutes between the imposed shear history and the subsequent 3D imaging of bubble suspensions, to avoid any ageing of bubbles in between, so that the characterization of bubble size and suspension microstructure is as

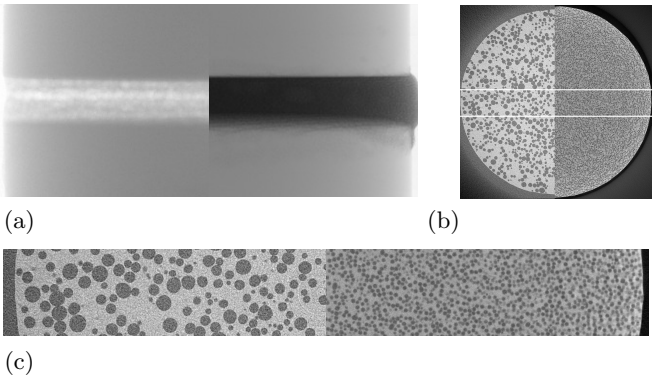

(a) (b)

(c)

FIG. 3. The materials shown here are the elasto-plastic suspensions of bubbles (1) on the left at a solid fraction $\phi \simeq 30\%$ and of particles (3) on the right at $\phi \simeq 35\%$. (a) X-ray radiograph corresponding to the transmitted intensity of X-rays through the suspensions within the parallel plates cell along one linear path. (b) Reconstructed horizontal slice encoding for X-ray absorption of voxels in the shear cell. (c) Zoom on the white rectangle drawn in (b). The dark discs on (b) and (c) are, respectively, the air bubbles and the PS particles.

close as possible to that induced by the shear history. To this aim, the different shear histories have been imposed to bubble suspensions (1) *in-situ* just before 3D imaging.

2. *Pair distribution function*

High definition 3D images (associated with subvoxel identification of solid particle centers [29], but with a precision of 1 voxel only for bubble centers) and large statistics based on numerous inclusions (150 000 solid particles, but 7 500 bubbles imaged in the whole gap) allow to investigate the microstructure at the inclusion scale, *i.e.* the spatial distribution of inclusions in the suspension. A relevant quantity to describe the suspension microstructure is the pair distribution function (pdf) $g(\vec{r})$, that is the probability of finding a pair of inclusions whose centers are separated by the vector $\vec{r}$, normalized by the mean particle density. For the quasi monodisperse solid particle suspensions, the pair vector $\vec{r}$ (and its coordinates) is normalized by the mean diameter d of the inclusions. For the polydisperse bubble suspensions, $\vec{r}$ is normalized by the sum of each pair inclusion radii. In both cases, it is denoted as $\vec{r}/d$ when normalized. Furthermore, to tackle the effect of the bubble polydispersity on the computed pdf, we consider only bubbles with a diameter between 100 and 500 μm, without any bubble in their close neighbourhood ($\|\vec{r}\| \leq 2.5$) outside of this diameter range (Fig. 15 in Appendix A). This reduces the number of analyzable bubbles in the whole gap to 4 000.

We focus on the suspension microstructure in the velocity-velocity gradient plane of the simple rotational shear flow imposed locally by the geometry, that is, respectively along the azimuthal axis and the vertical axis. To do so, we compute the 2D pdf $g_r(\ell, \xi)$, with (ℓ, ξ) the

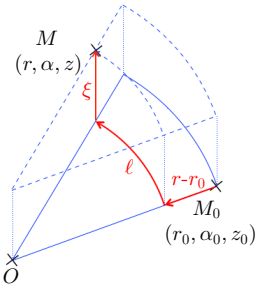

FIG. 4. Two inclusions $M_0\,(r_0, \alpha_0, z_0)$ and $M\,(r, \alpha, z)$ in the global cylindrical frame, separated by the pair vector $\vec{r} \equiv \overrightarrow{M_0M}$ defined in curvilinear coordinates (along circular flow lines): $\vec{r} = (r - r_0,\, \ell,\, \xi)$ with $\ell = r(\alpha - \alpha_0)$ and $\xi = z - z_0$.

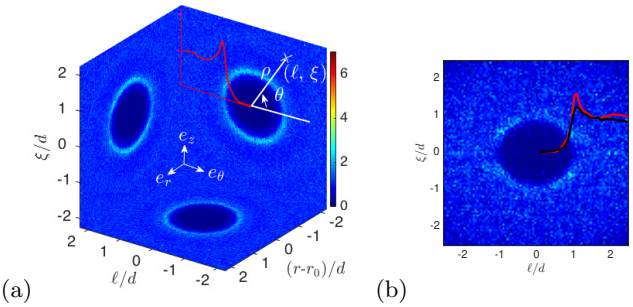

(a) (b)

FIG. 5. (a) Color maps of the 2D pdfs in the three orthogonal cylindrical planes $g_r(\ell, \xi)$, $g_\theta(r - r_0, \xi)$ and $g_z(r - r_0, \ell)$ for the particle suspension (3) at $\phi \simeq 35\%$ within an unsheared drop poured on a plate [29]. In the azimuthal plane, polar coordinates of the pair vector are defined in the local frame so that $\ell = \rho \cos\theta$ and $\xi = \rho \sin\theta$. (b) The 2D pdf $g_r(\ell, \xi)$ in the azimuthal plane for the bubble suspension (1) at $\phi \simeq 30\%$ within an unsheared drop poured on a plate. In (a) and (b), the continuous (red and black) curves show the average of $g_r(\rho, \theta)$ over all θ for both suspensions; in (b) is superimposed the average for the particle suspension (red).

cylindrical coordinates of a pair located in the velocity-velocity gradient plane $r = r_0 \pm d/2$: $\ell = r(\alpha - \alpha_0)$ and $\xi = z - z_0$ with (r, α, z) and (r_0, α_0, z_0) the inclusion cylindrical coordinates (Fig. 4). Alternatively to the global cylindrical coordinates (ℓ, ξ), one may use the polar coordinates (θ, ρ), defined as $\ell = \rho \cos\theta$ and $\xi = \rho \sin\theta$ [Fig. 5(a)] with the velocity axis ($\xi = 0$) used as the origin of the polar angle ($\theta = 0°$). In order to characterize the microstructure for a roughly homogeneous simple shear, we compute the pdf at a fixed radial position R_0 in the parallel plates geometry. In practice, to get a good precision on the pdf, a toroidal region of sufficient thickness ΔR is analysed. This leads us to choose $R_0 = 0.72D/2 \pm 0.12D/2$. Obviously, the pdf $g_r(\ell, \xi)$ is symmetric according to the origin ($\ell = 0$, $\xi = 0$) due to rotational shear flow symmetry.

An example of 2D pdfs in the three orthogonal cylindrical planes $g_r(\ell, \xi)$, $g_\theta(r - r_0, \xi)$ and $g_z(r - r_0, \ell)$ is given in Fig. 5a for the particle suspension (3) at $\phi \simeq 35\%$ within a drop [29], which is just poured on a plate and

thus unsheared. Before any loading or shear history, we observe that the material is isotropic, showing a circular symmetry in each plane and being the same in the three orthogonal planes. The same is qualitatively observed for the bubble suspension (1) at $\phi \simeq 30\%$ from the 2D pdf $g_r(\ell, \xi)$ in Fig. 5b, although the lower precision on the bubble centers, the smaller statistics and the size polydispersity lead to a slightly blurry pdf [48]. In any case, the average of $g_r(\rho, \theta)$ over all θ, shown by continuous (red and black) curves in Fig. 5, is approximately the same for both suspensions [49]. More details are given in Deboeuf *et al.* [29].

III. PARTICLE-INDUCED STRAIN HARDENING

In this section, we focus on the elasto-plastic behavior of the materials. The crucial role of particles on strain hardening is evidenced by comparing the solid particle suspensions to the pure suspending elasto-plastic fluid and to the bubble suspensions. We investigate their stress *versus* strain response to shear-stress-controlled and shear-rate-controlled tests in Sec. III A. To disentangle the evolutions of elasticity and plasticity in this response, we subsequently determine both their current yield stress and their current elastic modulus throughout their transient hardening in Sec. III B.

A. Stress-strain response

The $\tau(\gamma)$ response of all the samples (pure fluid and suspensions) to a quasi-static shear flow is typical of an elasto-plastic behavior in shear-stress-controlled (Fig. 6) as well as in shear-rate-controlled (Fig. 7) tests. The stress first increases linearly with the strain at low strain (likely corresponding to an elastic regime); the stress/strain slope then decreases progressively until a plastic plateau is reached. The observed transient behavior is the hallmark of strain hardening. As discussed below, its exact characteristics depend much on the material and on its shear history.

In order to characterize quantitatively strain hardening, we define the characteristic hardening shear strain γ_h as the plastic strain accumulated when τ reaches $0.9\tau_Y^\infty$. To better compare the various responses, it is convenient to use rescaled stress and strain units as:

$$\tilde{\tau} = \tau/\tau_Y^\infty \tag{2}$$

and

$$\tilde{\gamma} = \gamma\, G'^\infty/\tau_Y^\infty, \tag{3}$$

Within this set of units, a perfect elasto-plastic behavior is $\tilde{\tau} = \tilde{\gamma}$ for $\tilde{\gamma} \leq 1$ and $\tilde{\tau} = 1$ for $\tilde{\gamma} \geq 1$, and the characteristic hardening shear strain $\tilde{\gamma}_h$ is the rescaled plastic strain accumulated for $\tilde{\tau} = 0.9$; in practice, this plastic strain is estimated by substracting the linear elastic strain $\tilde{\gamma}_e = 0.9$ to the strain $\tilde{\gamma}$ reached at $\tilde{\tau} = 0.9$ on the $\tilde{\tau}(\tilde{\gamma})$ loading curve. $\tilde{\gamma}_h^-$ and $\tilde{\gamma}_h^+$ are the characteristic hardening shear strains observed, respectively, for the two initial pre-shear conditions $-$ and $+$. The Bauschinger effect can then be quantified by $\Delta\tilde{\gamma}_h = \tilde{\gamma}_h^- - \tilde{\gamma}_h^+$. The values of $\tilde{\gamma}_h^-$, $\tilde{\gamma}_h^+$, and $\Delta\tilde{\gamma}_h$ determined for two different emulsions, a suspension of bubbles and two suspensions of particles are reported in Tab. II and commented below.

1. Pure emulsion

For a pure concentrated emulsion (Figs. 6a and 7a), the different initial conditions (pre-shear + and pre-shear $-$) do not change the steady yield stress τ_Y^∞ and only slightly change the characteristic hardening shear strain γ_h ($\gamma_h^- \simeq 2\gamma_h^+$). This slight effect is due to the alteration under shear flow of the microstructure of the elasto-plastic fluid at the scale of its composing droplets [50]. Moreover, in a controlled shear-rate mode, an overshoot of the stress $\tau > \tau_Y^\infty$ is observed before reaching the steady plastic flow for pre-shear + [Fig. 7(a)]. However, the strain γ_h for the strain hardening observed here (and studied recently in the literature [19, 51, 52]) and $\Delta\gamma_h$ for the Bauschinger effect are very small (only a few %), and as shown below, are not significant compared to those induced by the presence of solid particles; this will not be discussed further in the paper. For our concern, the suspending fluids – the emulsions – can be considered as model elasto-plastic materials.

2. Bubble suspension

Figure 6b shows the stress-strain response of the bubble suspension (0) at a volume fraction $\phi \simeq 37\%$ for the two initial conditions pre-shear + and $-$. Its mechanical response is only slightly modified upon a shear reversal, as for the pure fluid ($\phi = 0$) [Fig. 6(a)]: the bubble suspension does neither exhibit significant Bauschinger effect nor significant strain hardening. When rescaled units $\tilde{\tau}$ and $\tilde{\gamma}$ are used [Figs. 6(d) and (e)], which accounts for the possible decrease of the elastic modulus when adding bubbles [53], the emulsion and the bubble

TABLE II. Rescaled values of the characteristic hardening shear strains $\tilde{\gamma}_h^-$ and $\tilde{\gamma}_h^+$, and $\Delta\tilde{\gamma}_h = \tilde{\gamma}_h^- - \tilde{\gamma}_h^+$ for 5 different materials.

Sample	$\tilde{\gamma}_h^+$	$\tilde{\gamma}_h^-$	$\Delta\tilde{\gamma}_h$
Pure fluid (i)	3	6	3
Pure fluid (ii)	1	2	1
(0): $\phi = 37\%$ bubbles in (i)	4	9	5
(2): $\phi = 40\%$ solid part. in (i)	2	50	48
(3): $\phi = 35\%$ solid part. in (ii)	2	48	46

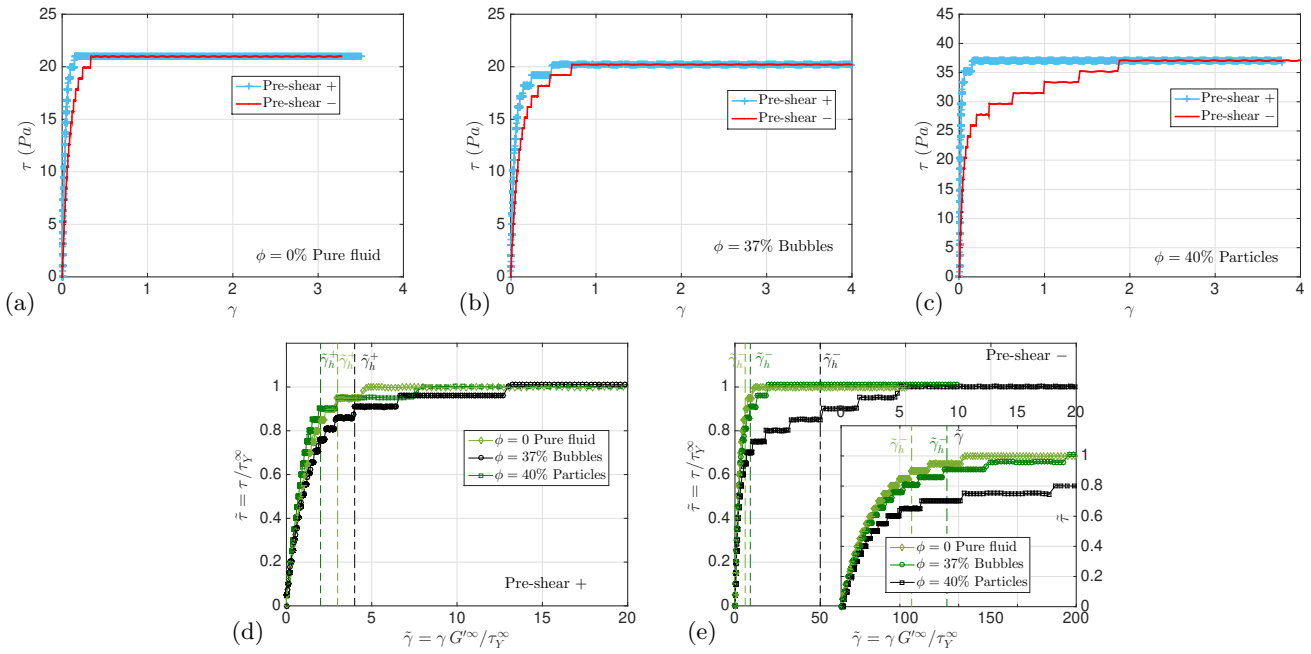

FIG. 6. (a)-(c) Stress-strain $\tau(\gamma)$ responses of (a) the pure fluid (i), (b) the bubble suspension (0) in the same fluid ($\phi \simeq 37\%$) and (c) the particle suspension (2) in the same fluid ($\phi \simeq 40\%$) to shear-stress-controlled tests, for the two initial conditions pre-shear + and pre-shear −. (d)-(e) Rescaled stress-strain $\tilde{\tau}(\tilde{\gamma})$ responses for the three samples for the initial conditions (d) pre-shear + and (e) pre-shear − (with a zoom in inset). Dashed lines show the characteristic rescaled plastic shear strain $\tilde{\gamma}_h$ so that $\tilde{\tau}(\tilde{\gamma}_h) = 0.9$.

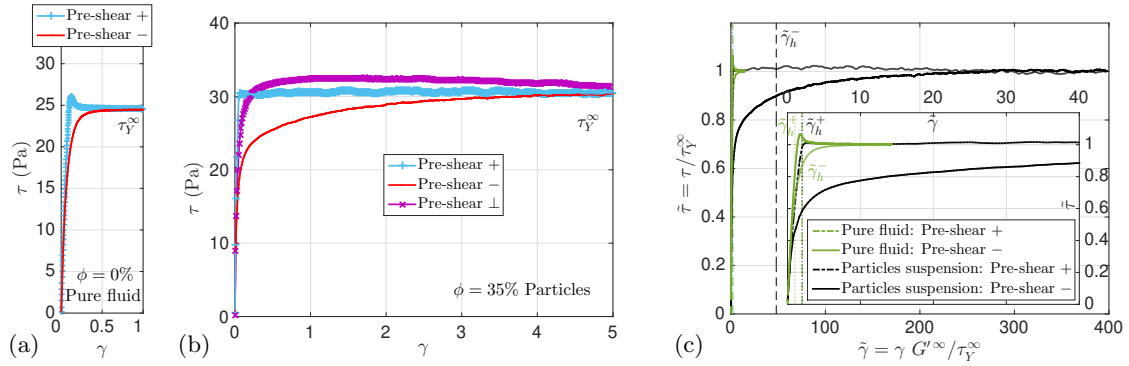

FIG. 7. (a)-(b) Stress-strain responses $\tau(\gamma)$ during a shear-rate-controlled test for (a) the pure suspending fluid (ii) and (b) for the particle suspension (3) in the same fluid ($\phi \simeq 35\%$) from different initial conditions: pre-shear +, pre-shear − and pre-shear ⊥. (c) Comparison of these responses on the same plot with the help of rescaled units $\tilde{\tau} = \tau/\tau_Y^\infty$ and $\tilde{\gamma} = \gamma\, G'/\tau_Y^\infty$, with a zoom in inset. Dashed lines show the characteristic rescaled plastic shear strain $\tilde{\gamma}_h$ so that $\tilde{\tau}(\tilde{\gamma}_h) = 0.9$.

suspension appear to have very close behavior in both cases (pre-shear − and pre-shear +). Remarkably, the rescaled values of the difference $\Delta\tilde{\gamma}_h$ between the characteristic hardening shear strains are similar, of the order of 4, in the suspension of bubbles as in the emulsion (see Tab. II).

The same is observed whatever the volume fraction ϕ of bubbles is (see the rescaled stress-strain responses for different bubble volume fractions ϕ from 0% to 44% in Fig. 16a and b, Appendix B). This is obvious in Fig. 8 where the difference of rescaled characteristic hardening shear strains $\Delta\tilde{\gamma}_h$ is observed to be low and independent of the bubble volume fraction ϕ. All the deviation from a perfect elasto-plastic behavior observed in the bubble suspensions can thus be attributed to the suspending emulsion. To conclude, the bubbles and their interactions do neither induce any significant strain hardening nor any Bauschinger effect.

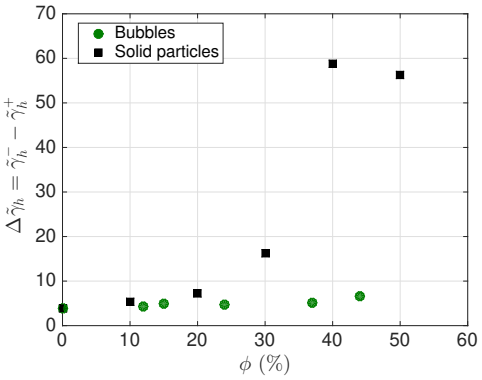

FIG. 8. Bauschinger effect: rescaled difference $\Delta\tilde{\gamma}_h = \tilde{\gamma}_h^- - \tilde{\gamma}_h^+$ between the characteristic hardening shear strains for the two initial pre-shear conditions ($-$ and $+$) as a function of the volume fraction ϕ of solid particles (2) – in black squares – or bubbles (0) – in green circles – dispersed in the same elasto-plastic fluid (i).

3. *Particle suspension*

PS spheres (2) and (3) have been added in the concentrated emulsion (i) and (ii) at a volume fraction $\phi \simeq 35\%$ and 40% respectively (Figs. 6c and 7b). In the presence of particles, different initial conditions (pre-shear $+$, $-$ and $\perp$) now lead to significantly different stress-strain curves. The steady yield stress τ_Y^∞ is the same for all the initial conditions. However, the characteristic hardening shear strain γ_h before reaching the steady plastic flow is strongly dependent on the initial condition: whereas γ_h^+ is a few % for pre-shear $+$, the characteristic shear strain γ_h^- is very large, of the order of 1, for pre-shear $-$, leading to a dramatic increase of the difference $\Delta\gamma_h$ accounting for the Bauschinger effect as compared to the suspending emulsion. By comparison, the suspension pre-sheared in an orthogonal direction (pre-shear $\perp$) has only little hardening with $\gamma_h^\perp \simeq 0.1$ [Fig. 7(b)].

The rescaled $\tilde{\tau}(\tilde{\gamma})$ curves displayed in Fig. 7c for the pure suspending emulsion (ii) and for the particle suspension (3), clearly show that particles suspended in the elasto-plastic fluid present a very specific response to shear reversal, which is dramatically different from the limited Bauschinger effect found in the pure fluid and in the bubble suspensions (see also Fig. 6e). Whereas very close behaviors are observed for all materials with the initial condition pre-shear $+$, the steady plastic behavior for the particle suspension with the initial condition pre-shear $-$ is reached for a rescaled strain $\tilde{\gamma}_h^-$ of the order of 50 for $\phi \simeq 35\%$, 10 times larger than for the other samples (see Tab. II).

The volume fraction ϕ of solid particles (2) suspended in the fluid (i) has been systematically varied from 0% to 50% for the two initial conditions pre-shear $+$ and $-$ (see Fig. 16c and d in Appendix B). The initial condition has a strong influence on the elasto-plastic response of solid particle suspensions for solid fractions $\phi \gtrsim 30\%$. Figure 8 shows the rescaled difference $\Delta\tilde{\gamma}_h$ as a function of the volume fraction ϕ: the larger ϕ is, the larger the Bauschinger effect is. A dramatic increase of the characteristic hardening strain $\tilde{\gamma}_h^-$ and of $\Delta\tilde{\gamma}_h$ is observed when $\phi \gtrsim 30\%$, with $\Delta\tilde{\gamma}_c \sim 50$ for $\phi \simeq 50\%$. This is in strong contrast with the behaviour of bubble suspensions. To conclude, the solid particles and their interactions induce a significant strain hardening for a preshear $-$ and a dramatic Bauschinger effect, which are not observed in the pure suspending emulsion.

B. Current yield stress and elastic modulus

To better characterize the strain hardening induced by the solid particles, a suspension (3) at a solid fraction $\phi \simeq 35\%$ is submitted to a quasi-static plastic flow in a shear-rate-controlled test associated with systematic unload-reload steps (see Sec. II B 3). Its stress-strain response is shown in Fig. 9a by the colored curves for the initial condition pre-shear $-$, the furthest one from the steady state. For comparison, the response to the same flow without unload-reload steps is shown in black: both methods give the same macroscopic response, showing that this experiment is not perturbative. The dotted black curve corresponds to a flow from the initial condition pre-shear $+$. At a given accumulated plastic deformation γ_p, the two straight (colored) lines corresponding to unload and reload superimpose nearly perfectly, showing that unload and reload happen elastically for stresses below the current yield stress $\tau_Y(\gamma_p)$. This demonstrates that the stress-strain curve reflects the current yield stress evolution with the accumulated plastic strain. The same holds for a shear-stress-controlled test.

Figure 9b shows the current yield stress $\tau_Y/\tau_Y^\infty(\gamma_p)$ and elastic modulus $G'/G'^\infty(\gamma_p)$, rescaled by their steady values, for different accumulated plastic deformation γ_p. When pre-sheared in the opposite direction, the suspension has low initial values of G' and τ_Y, which increase transiently until their steady values, contrary to the case of a suspension pre-sheared in the same direction, which keeps constant elasto-plastic properties.

However, the decrease upon reversal of τ_Y is abrupt with a discontinuity, whereas the quick decrease of G' is continuous. This is clearer when measuring continuously the elastic modulus $G'(\gamma_p)$ as a function of the deformation γ_p for a shear-reversal experiment (pre-shear $-$ initial state) in stress-controlled experiments thanks to superposition of oscillations (see Sec. II B 3), as shown in Fig. 10.

The same stress-controlled experiments have been performed for the pure fluid (i), the bubble suspension at $\phi \simeq 30\%$ (0) and the solid particle suspension at $\phi \simeq 37\%$ (2). The dimensionless $G'/G'^\infty(\gamma)$ data of all materials are plotted in Fig. 10. Note that in this case, G' is initially larger than at steady-state in all materials because it is measured at zero stress initially whereas it is measured around $\tau = \tau_Y^\infty$ at steady-state: this difference

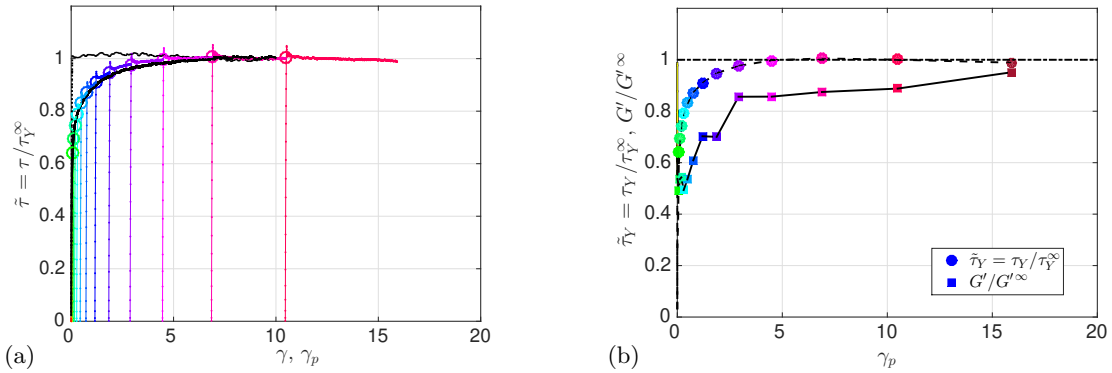

FIG. 9. (a) Stress-strain $\tilde{\tau}(\gamma)$ response of a particle suspension (3) from the initial condition pre-shear $-$ during a shear-rate-controlled test associated with load-unload-reload steps. The black continuous curve is the stress-strain response to the same flow without load-unload-reload steps, whereas the black dotted one corresponds to a flow from the initial condition pre-shear $+$. (b) Current yield stress $\tau_Y/\tau_Y^\infty(\gamma_p)$ (circles) and elastic modulus $G'/G'^\infty(\gamma_p)$ (squares) at different accumulated plastic deformation γ_p, rescaled by their steady values.

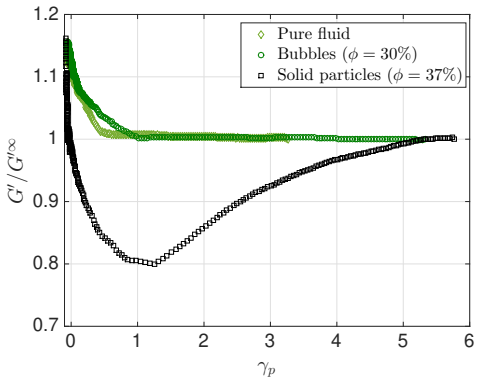

FIG. 10. Current elastic modulus G'/G'^∞ measured in controlled-shear-stress experiments, rescaled by its steady value, as a function of the deformation γ_p in a shear-reversal experiment (initial state: pre-shear $-$) for a pure elasto-plastic fluid, a solid particle suspension and a non-deformable bubble suspension at similar volume fractions $\phi \approx 35\%$.

only reflects the nonlinear elasticity of the material for a same state.

The first important feature observed in these elastic modulus measurements during shear-reversal experiments is that the response of the pure emulsion and that of the bubble suspension superimpose. Again, this shows that the bubbles do not induce any strain hardening in the elastoplastic emulsion; the only impact of the bubbles is a change in the values of the macroscopic properties [36, 53]. These responses are very different from that observed in the particle suspension. All the slow non-monotonous evolution of G'/G'^∞ below 1 for the particle suspension (2) can be attributed to the presence of the particles. In addition to the dramatic strain hardening and Bauschinger effect, the elasto-plastic suspensions are shown here to exhibit significant softening, with a huge typical deformation of about 2.5 necessary for the current elastic modulus G' to reach $0.9G'^\infty$ (6 to recover its steady value G'^∞). These typical deformations are much larger than the characteristic hardening shear stress $\gamma_h^- \sim 1$ for the current yield stress τ_Y to reach $0.9\tau_Y^\infty$ (~ 2 to reach its steady value). This observation holds for both shear-stress-controlled (Figs. 6(c) and 10) and shear-rate-controlled tests [Fig. 9(b)].

All these experiments finally demonstrate the major role of the solid particles in the development of strain hardening and softening, in addition to their well-known effect on the steady mechanical properties [38, 39]. This highlights the crucial role of their evolving microstructure on the suspension behavior, which we investigate in the next section.

IV. SHEAR-HISTORY DEPENDENT MICROSTRUCTURE

To look for microscopic mechanisms responsible for the dramatic hardening and softening of solid particle suspensions, we investigate the spatial distribution of the particles for different shear histories (see Sec. II C 2). We focus on particle suspension microstructures during stationary flows and upon shear reversal. We also provide for the first time – according to our knowledge – a characterization of a bubble suspension microstructure. We recall that both types of suspensions (solid particles and air bubbles) have similar isotropic microstructures before any loading, as shown in unsheared drops poured on a plate (Fig. 5).

A. Particle suspensions

Figure 11 shows a selection of color maps of pdfs in the velocity-velocity gradient plane of the simple rotational shear flow $g_r(\ell, \xi) \equiv g_r(\rho, \theta)$ for a suspension of

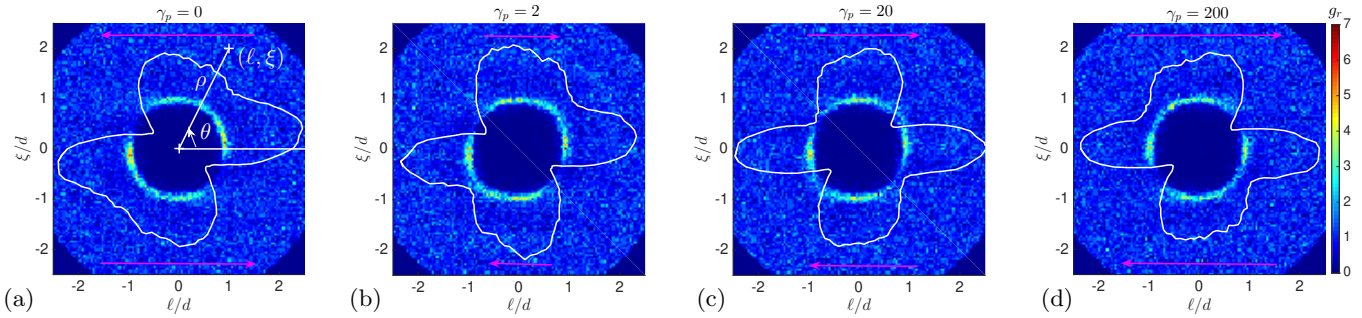

FIG. 11. Color maps of pair distribution functions $g_r(\ell, \xi) \equiv g_r(\theta, \rho)$ in the velocity-velocity gradient plane of the simple shear flow imposed locally by a parallel plates geometry for a suspension (3) of $\phi \simeq 35\%$ particles in the concentrated emulsion (ii). The four maps correspond to different accumulated plastic deformation $\gamma_p = 0$, 2, 20 and 200 since the initial condition (pre-shear −). The first map ($\gamma_p = 0$) corresponds to the steady state for a suspension presheared in the opposite direction. The two arrows symbolise the direction of flow and the amplitude of the strain experienced up to the imaging.

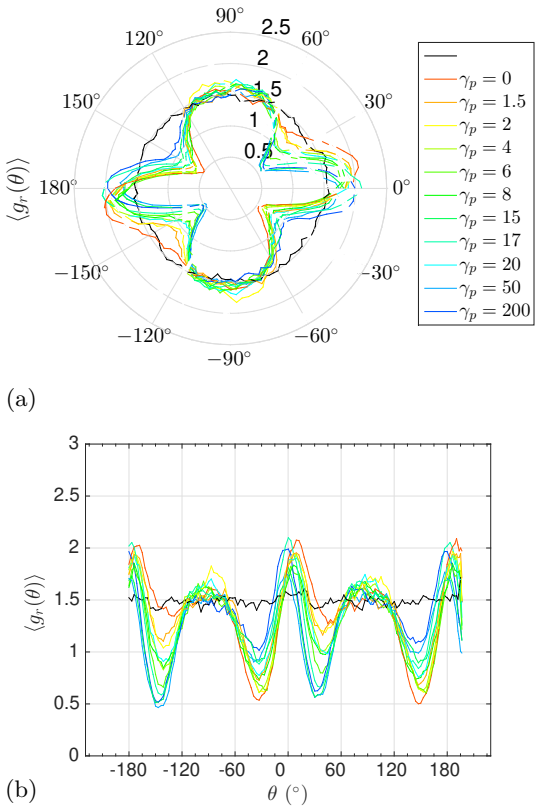

FIG. 12. Pdf g_r averaged over pairs of distance ρ equal to $d \pm d/6$, d being the particle diameter: $\langle g_r(\theta) \rangle$, for different shear history (γ_p from 0 to 200). The black curve refers to an isotropic pdf measured in a suspension drop, which was not pre-sheared. Two representations are shown: (a) in a polar frame ($\langle g_r(\theta) \rangle \cos\theta$, $\langle g_r(\theta) \rangle \sin\theta$) and (b) in a Cartesian frame (θ, $\langle g_r(\theta) \rangle$).

$\phi \simeq 35\%$ particles in a concentrated emulsion (3). These maps correspond to the accumulated plastic deformation $\gamma_p = 0$, 2, 20 and 200 in a shear-reversal experiment (pre-shear −). The first (a) and last (d) maps thus correspond to steady microstructures for shear flows in two opposite directions; in-between, maps correspond to intermediate microstructures during hardening. For particles separated by large distances ρ, the pdf g_r is homogeneously equal to 1, which implies the absence of any long range organisation. All the angular and temporal variations of the microstructure occur for particles in contact or close to contact for which $g_r(\rho \simeq d) \neq 1$.

A finer description is thus possible by computing the radial average $\langle g_r(\theta) \rangle$ for distances ρ corresponding to its maxima ($\rho = d \pm d/6$), that is, in or close to contact (superimposed on Fig. 11). We emphasize that it is not possible to distinguish experimentally particles that are actually in direct contact from those separated by a thin fluid layer. Two representations are used to plot the function $\langle g_r \rangle$: either in a polar plot, where the coordinates are ($\langle g_r(\theta) \rangle \cos\theta$, $\langle g_r(\theta) \rangle \sin\theta$), or in an "unrolled" Cartesian plot, where the coordinates are (θ, $\langle g_r(\theta) \rangle$), as shown in Fig. 12 for many different values of the plastic deformations γ_p (between 0 and 200) accumulated since the initial condition (pre-shear −). The averaged pdf for an isotropic microstructure is also plotted in black in Fig. 12 [29]: at contact, due to excluded volume effects, there is an excess of particle pairs as compared to long distance, and $g_r \simeq 1.5$ [54]. Over-population and depletion of particle pairs can thus be identified, respectively, with $g_r > 1.5$ and $g_r < 1.5$.

Stationary state. The initial steady microstructure [Fig. 11(a)], shows a shear-induced anisotropic state, characterized by different values of $g_r(\rho \simeq d)$ in or close to contact in the domains of compression ($0° \leq \theta \leq 90°$) and tension ($90° \leq \theta \leq 180°$) of the simple shear flow. More precisely, the initial pdf $\langle g_r(\theta) \rangle$ shows two main features. (1) There is a major over-population region ($g_r \simeq 2$) for $\theta = 10°$, which can be described as an alignment with the flow as $\theta \approx 0°$; this overpopulation region extends over one third of the compression region (*i.e.* for $0° \lesssim \theta \lesssim 30°$). (2) There is a major depletion region in the tension region ($g_r \simeq 0.5$), aligned with the direction $\theta = 150°$; this depletion region extends over two third of the tension region (*i.e.* for

$120° \lesssim \theta \lesssim 180°$). Particle pairs in (or close to) contact oriented along $60° \lesssim \theta \lesssim 120°$ are statistically as present as in an isotropic microstructure ($g_r \simeq 1.5$). We also note that there is a slight region of depletion as compared to the isotropic structure (with $g_r \simeq 1.2$) for $30° \lesssim \theta \lesssim 60°$.

The steady microstructure in Fig. 11d corresponding to the steady state under the reference direction is the mirror of the initial one: the two pdfs are symmetric according to the $\ell = 0$-axis as expected from the flow symmetry. Thus, the main differences between the two mirror steady pdfs lie in the switch of directions between $\theta = 150°$ and $\theta = 30°$ for the main depletion region and in the slight 'rotation' of the direction of the over-population aligned with the flow (*i.e.* from $\theta \approx 10°$ to $\theta \approx -10°$), whereas $\langle g_r(60° \lesssim \theta \lesssim 120°)\rangle$ keeps roughly constant and close to 1.5.

This anisotropy, with a depleted zone in the tension region, is referred to in the literature as a fore-aft asymmetry; it is the hallmark of suspensions of rough rigid particles [27] (see Sec. I). It reflects the existence of a cut-off in the hydrodynamic repulsive force due to particle roughness and to the fact that interparticle contact forces exist only in compression [28, 30, 31]. In addition, for a nonlinear interstitial fluid, this steady-state microstructure slightly depends on the applied shear rate; this is discussed in detail elsewhere [29, 31, 33]: our focus here is on the impact of shear history.

Shear reversal. Obviously, during a shear reversal the particle pair distribution has to evolve from a steady state to its mirror. It is actually observed that the microstructure slowly changes and progressively 'rotates'. Figure 12a shows that the fraction of particle pairs similar to the isotropic case ($60° \lesssim \theta \lesssim 120°$) does not change significantly during a shear reversal, while the maximum of over-population direction slightly 'rotates' from $\theta \approx 10°$ to $\theta \approx -10°$. In the same time, the two observed depletion regions are progressively switched: Figure 12b shows that g_r in the major and minor depletion regions respectively increase and decrease (but not simultaneously), leading to a switch in the direction of the main depletion region from $\theta = 150°$ to $\theta = 30°$. The minor depletion region in the compression region ($90° \leq \theta \leq 180°$) for $\gamma_p = 200$ is likely a reminiscence of the previous depletion of particle pairs, which might become even slighter, at longer strain scales. Some additional characterization of the evolution of the microstructure of the solid particle suspension during a shear reversal is given in Appendix C (see Fig. 17 and 18).

B. Bubble suspension: steady-state

Figure 13 shows the 2D pdf g_r in the velocity-velocity gradient plane of the simple rotational shear flow for a bubble suspension (2) of $\phi \simeq 37.5\%$ volume fraction, after a plastic shear, with $\gamma_p \simeq 24$, at a shear rate $\dot{\gamma} \simeq 0.8$ s^{-1}. We recall that distances ρ between pairs of bubbles have been normalized by the sum of their radii to take into account the bubble polydispersity (see Sec. II C 2). This pdf measured just after a steady shear flow (to avoid any change of the bubble size and position between their shear and their imaging) is very different from that measured in an unsheared drop [Fig. 5(b)].

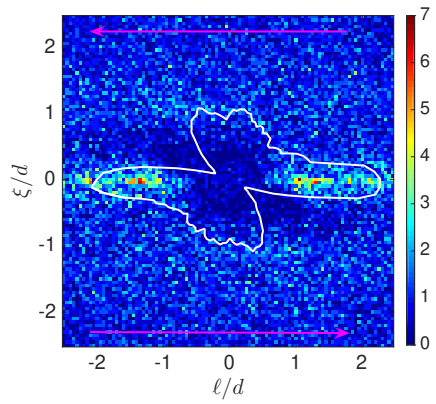

FIG. 13. Color map of the pdf g_r in the velocity-velocity gradient plane of the simple shear flow imposed locally by a parallel plates geometry for the bubble suspension (1) of $\phi = 37.5\%$ volume fraction in the concentrated emulsion (i). Pair distances ρ between bubbles have been normalized by the sum of their radii.

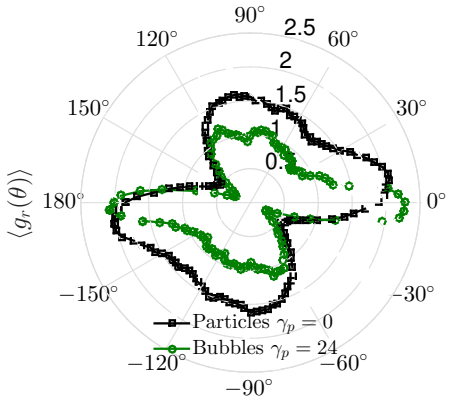

FIG. 14. Pdf $\langle g_r(\theta)\rangle$ averaged over pairs of distance ρ normalized by the sum of radii equal to $1 \pm 1/6$ in a polar frame for the sheared bubble suspension (1) ($\phi \simeq 37.5\%$) superimposed to the steady shear-induced pdf of a solid particle suspension ($\phi \simeq 35\%$).

Most important, it is drastically different from that measured for a solid particle suspension. In the bubble suspension, the variations of g are not localized to the region around $\rho \simeq d$ within a circular ring, *i.e.* at (or close to) contact. Its main characteristics are the symmetric alignment of bubble pairs exactly with the flow ($\xi = 0$) and the existence of a wide zone with fore-aft asymmetry, with bubble depletion, extending to large ρ values.

Although all the information of the bubble suspension

pdf is not only localized around $\rho \simeq d$, contrary to the particle suspension pdf, it is useful to compute the average $\langle g_r(\theta)\rangle$ for bubble pairs in or close to contact (*i.e.*, for distances ρ normalized by the sum of the bubble radii equal to $1 \pm 1/6$) for a quantitative comparison of the microstructure of bubble and solid particle suspensions. The average $\langle g_r(\theta)\rangle$ for bubble suspension is superimposed on the 2D pdf colormap in Fig. 13. Figure 14 also shows the average $\langle g_r(\theta)\rangle$ for bubbles superimposed to that of solid particles in a suspension of similar volume fraction ϕ, in the steady shear-induced anisotropic state. These curves present strong differences, showing that the physics at play in both systems is radically different. In particular, by contrast with particle suspensions, for which there is an excess of particles in the whole compression quadrant, the zone of bubble accumulation at contact is limited to $\theta \simeq 0$, pointing to bubble alignment.

V. DISCUSSION AND CONCLUSION

Dispersing solid hard particles in an elasto-plastic material leads to important shear-history dependence of the behavior, namely strain hardening. It is observed here to be particularly dramatic in a shear-reversal experiment.

During a shear reversal, the variations of both the elasto-plastic properties and the microstructure of solid particle suspensions happen in parallel. This observation is reminiscent of the viscosity change upon shear reversal in viscous suspensions [34, 55], which is also reflected in a microstructure change [56], with features similar to those we report here. As in this latter case, it is likely that the microstructure evolution reflects the abrupt opening of the contacts upon reversal in the tension region (which was the compression region before reversal) as well as the progressive accumulation of contacts in the compression region (the depleted tension region before reversal), as shown in numerical simulations of viscous suspensions [55]. In concentrated suspensions, contacts play indeed a major role in the stresses developed by a suspension under shear [57], and any change in the contact distribution has a dramatic impact on the mechanical properties.

We note however that the pdf evolves over a larger strain scale than the rheological properties: a transient symmetric microstructure [Fig. 11(c)] is observed for a plastic strain of the order of 20 for which the steady yield stress and the steady elastic modulus have already been reached, whereas a plastic strain of the order of 200 is needed to reach a steady microstructure. It is likely due to the fact that the experimental pdf captures both particles in contact and particles separated by a thin fluid layer: contacts are formed more rapidly and have the main impact on the mechanical properties.

The role of the solid particle interactions in strain hardening is highlighted thanks to the comparison with suspensions of non-deformable bubbles. As shown here, the bubbles do not induce any additional history dependence to the emulsion elasto-plastic behavior. Two main differences may be at the origin of this difference with solid particles: (1) bubbles are smooth, which may prevent the formation of contacts; (2) there is no static friction force between two bubbles. Bubbles can thus be considered as smooth frictionless particles. From the literature of suspensions, it seems that the roughness is crucial in the development of fore-aft asymmetry [28, 30]. The smoothness of the bubbles is thus likely the main point explaining the absence of strain hardening in bubble suspensions. Based on this argument, one could expect the bubble suspension to develop a symmetric microstructure, which is not what we observe here. However, the microstructure of bubble suspensions is dramatically different from that of particle suspensions. The fore-aft asymmetry is limited to the contact region for the solid particle suspensions, whereas it extends far from contact for the bubble suspension. This points to a hydrodynamic origin of this asymmetry in the case of bubbles. As visco-plastic interactions do not induce any asymmetry in the interaction of pairs of smooth particles [31], elasticity might additionally play a crucial role in the long-range asymmetry observed in the case of bubbles [32, 58].

To conclude, in this paper, by conducting both fine rheological experiments (steady characterization and shear reversal in elasto-plastic regimes) and microstructure characterization (thanks to 3D imaging) on suspensions of solid particles and bubbles, we have observed dramatic strain hardening, Bauschinger effect, softening and dependence on shear history attributed to the solid nature of inclusions. In particular, we have evidenced that this important shear-history dependence is related to shear-history dependent particle pair distribution functions. Roughness and interparticle contacts likely play a major role, as replacing hard particles by non-deformable bubbles suppresses strain hardening and modifies the suspension microstructure. Beyond suspensions, our study provides a new insight in the understanding and the control of strain hardening in composite materials.

ACKNOWLEDGMENTS

This work was supported by the Agence Nationale de la Recherche (grant ANR-10-JCJC-0905 SUSPASEUIL). The Laboratoire Navier microtomograph was acquired with the support of Region Ile-de-France (SESAME program) and F2M (Fédération Française de Mécanique).

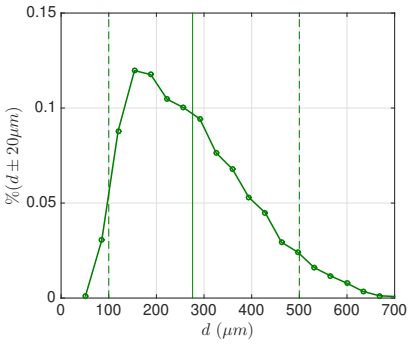

FIG. 15. Distribution of bubble (1) diameters. The average diameter is 280 μm (continuous line). The minimal (100 μm) and maximal (500 μm) bubble diameters considered for the computation of the pdf are shown by the dashed lines.

Appendix A: Bubble size distribution

Figure 15 shows the bubble (1) diameter histogram that we measured thanks to 3D imaging (X-ray tomography). These bubbles have a wide diameter distribution as they consist of bubbles (0) prepared ~ 1 h before imaging, due to incompressible delay times, so that they have aged since their preparation; this coarsening is a classical feature of foams [37]. However, special attention has been paid to the analysis of their microstructure to take into account their polydispersity: we consider only bubbles with a diameter between 100 and 500 μm, without any bubble in their close neighbourhood outside of this diameter range.

Appendix B: Shear-stress-controlled tests for bubble and particle suspensions

Figure 16 shows the rescaled stress-strain responses $\tilde{\tau}(\tilde{\gamma})$ to shear-stress-controlled experiments for the two initial conditions pre-shear + [(a) and (c)] and − [(b) and (d)], for two types of suspensions: bubble suspensions (2) [(a) and (b)] and solid particle suspensions (3) [(c) and (d)] for various volume fractions ϕ of inclusions from 0% to 50% in the same elasto-plastic fluid (i). For all bubble volume fractions, the initial condition pre-shear + and the initial condition pre-shear − lead to similar response, with non-significant Bauschinger effect. By contrast, for solid particles, increasing the particle volume fraction leads to stronger and stronger strain hardening for the initial condition pre-shear −, which demonstrates a remarkable Bauschinger effect related to the solid nature of the inclusions.

Appendix C: Microstructure

Figure 17 shows the angle θ_{min} of the depletion region of the microstructure (global minima of the pdf $\langle g_r \rangle$) as a function of the plastic deformation γ_p applied from the initial state pre-shear −. The change of the angle of the depletion region from $\theta = -30° \equiv 150°$ to $\theta = +30°$ is abrupt; it occurs here for a typical deformation γ_p of about 20, for which the microstructure looks symmetric according the $\ell = 0$-axis (see Fig. 11c).

Figure 18 shows the values of g_{min} at its two minima (at angles $\theta = 30°$ and $\theta = 150°$) as a function of the plastic deformation γ_p accumulated since the initial condition (pre-shear −). Initially, the depletion region in the tension region is aligned with $\theta = 150°$ and $\langle g_r(\theta = 150°) \rangle$ is minimal ($\simeq 0.5$); upon shear reversal, $\langle g_r(\theta = 150°) \rangle$ increases towards $\simeq 1$, while $\langle g_r(\theta = 30°) \rangle$ decreases below 1 until reaching $\simeq 0.5$. This demonstrates the transition of the main depletion region from 150° to 30°, while illustrating the kinetics of this transition.

[1] R. F. Landel and L. E. Nielsen, *Mechanical properties of polymers and composites* (CRC press, 1993).
[2] I. M. Daniel and O. Ishai, *Engineering Mech. of composite materials*, Vol. 1994 (Oxford university press New York, 2006).
[3] M. Vincent, T. Giroud, A. Clarke, and C. Eberhardt, Description and modeling of fiber orientation in injection molding of fiber reinforced thermoplastics, Polymer **46**, 6719 (2005).
[4] D. C. Hofmann, J.-Y. Suh, A. Wiest, G. Duan, M.-L. Lind, M. D. Demetriou, and W. L. Johnson, Designing metallic glass matrix composites with high toughness and tensile ductility, Nature (London) **451**, 1085 (2008).
[5] R. O. Ritchie, The conflicts between strength and toughness, Nature Mater. **10**, 817 (2011).
[6] J. Lemaitre and J.-L. Chaboche, *Mechanics of solid materials* (Cambridge University Press, 1994).
[7] A. Nadai, Plastic behavior of metals in the strain-hardening range. part i, J. Appl. Phys. **8**, 205 (1937).
[8] P. Hirsch, A theory of linear strain hardening in crystals, Discussions of the Faraday Society **38**, 111 (1964).
[9] Y. Wang and E. Ma, Strain hardening, strain rate sensitivity, and ductility of nanostructured metals, Mater. Sci. Eng.: A **375**, 46 (2004).
[10] J. Pan, Y. P. Ivanov, W. Zhou, Y. Li, and A. Greer, Strain-hardening and suppression of shear-banding in rejuvenated bulk metallic glass, Nature (London) **578**, 559 (2020).
[11] R. S. Hoy and M. O. Robbins, Strain hardening of polymer glasses: Entanglements, energetics, and plasticity, Phys. Rev. E **77**, 031801 (2008).
[12] W. Zou and R. G. Larson, A hybrid brownian dynam-

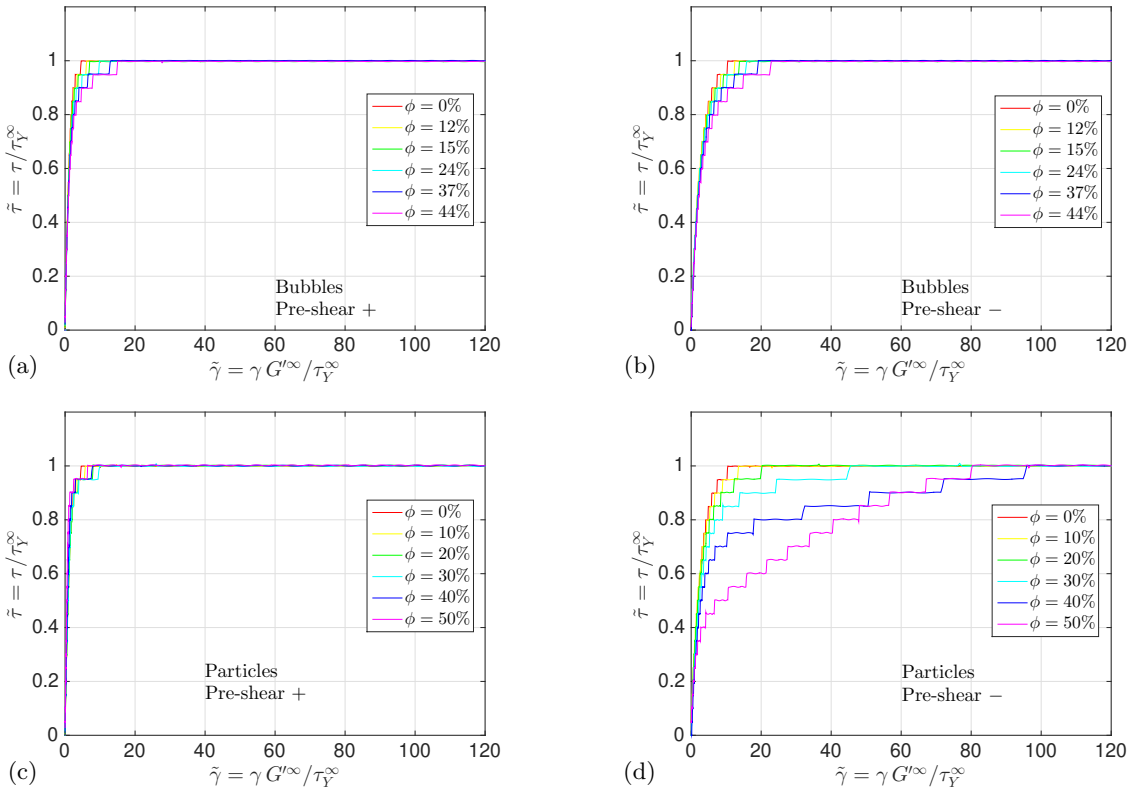

FIG. 16. Rescaled stress-strain responses $\tilde{\tau}(\tilde{\gamma})$ to shear-stress-controlled experiments for the two initial conditions pre-shear + [(a) and (c)] and − [(b) and (d)], for two types of suspensions: bubble suspensions (2) [(a) and (b)] and solid particle suspensions (3) [(c) and (d)] for various volume fractions ϕ of inclusions from 0% to 50% in the same elasto-plastic fluid (i).

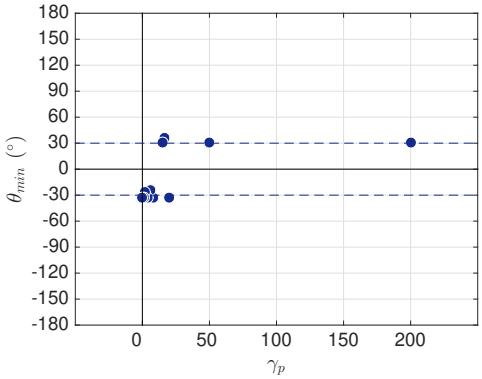

FIG. 17. Angle θ_{min} of the global minima of the pdf from $\langle g \rangle$ as a function of the plastic deformation γ_p accumulated since the initial condition (pre-shear −).

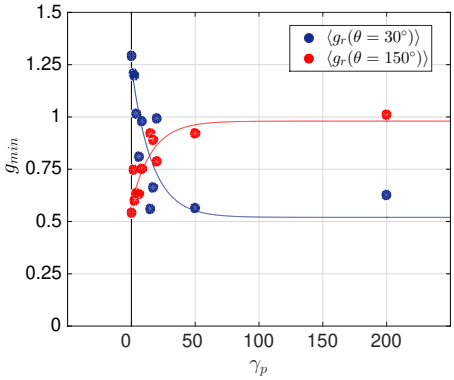

FIG. 18. Values of the pdf g_{min} at the local minima (at angles $\theta = 30°$ and $\theta = 150°$) as a function of the plastic deformation γ_p accumulated since the initial condition (pre-shear −).

ics/constitutive model for yielding, aging, and rejuvenation in deforming polymeric glasses, Soft Matter **12**, 6757 (2016).

[13] V. C. Li, S. Wang, C. Wu, *et al.*, Tensile strain-hardening behavior of polyvinyl alcohol engineered cementitious composite (pva-ecc), ACI Mater. Journal-American Concrete Institute **98**, 483 (2001).

[14] K. M. Weigandt, L. Porcar, and D. C. Pozzo, In situ neutron scattering study of structural transitions in fibrin networks under shear deformation, Soft Matter **7**, 9992 (2011).

[15] R. D. Groot, A. Bot, and W. G. Agterof, Molecular theory of strain hardening of a polymer gel: application to gelatin, J. Chem. Phys. **104**, 9202 (1996).

[16] H.-N. An, S. J. Picken, and E. Mendes, Direct observation of particle rearrangement during cyclic stress hard-

ening of magnetorheological gels, Soft Matter **8**, 11995 (2012).
[17] M. Laurati, S. Egelhaaf, and G. Petekidis, Plastic rearrangements in colloidal gels investigated by laos and ls-echo, J. Rheo. **58**, 1395 (2014).
[18] R. R. Vincent and P. Schurtenberger, Work hardening of soft glassy materials, or a metallurgist's view of peanut butter, Soft Matter **7**, 1635 (2011).
[19] C. J. Dimitriou, R. H. Ewoldt, and G. H. McKinley, Describing and prescribing the constitutive response of yield stress fluids using large amplitude oscillatory shear stress (laostress), J. Rheo. **57**, 27 (2013).
[20] A. K. Bhattacharjee, Stress–structure relation in dense colloidal melts under forward and instantaneous reversal of the shear, Soft Matter **11**, 5697 (2015).
[21] C. J. Dimitriou and G. H. McKinley, A canonical framework for modeling elasto-viscoplasticity in complex fluids, J. Non-Newt. Fluid Mech. **265**, 116 (2019).
[22] S. Buckley and K. Entwistle, The bauschinger effect in super-pure aluminum single crystals and polycrystals, Acta Metall. **4**, 352 (1956).
[23] R. Asaro, Elastic-plastic memory and kinematic-type hardening, Acta Metall. **23**, 1255 (1975).
[24] F. C. Frank, The frank—read source, Proc. R. Soc. Lond. A **371**, 136–138 (1980).
[25] F. Spaepen, Metallic glasses rejuvenated to harden under strain., Nature **578**, 521 (2020).
[26] P. Saramito, A new constitutive equation for elastoviscoplastic fluid flows, J. Non-Newt. Fluid Mech. **145**, 1 (2007).
[27] E. Guazzelli and J. F. Morris, *A Phys. introduction to suspension dynamics*, 45 (Cambridge University Press, 2011).
[28] F. Blanc, E. Lemaire, A. Meunier, and F. Peters, Microstructure in sheared non-brownian concentrated suspensions, J. Rheol. **57**, 273 (2013).
[29] S. Deboeuf, N. Lenoir, D. Hautemayou, M. Bornert, F. Blanc, and G. Ovarlez, Imaging non-brownian particle suspensions with x-ray tomography: Application to the microstructure of newtonian and viscoplastic suspensions, J. Rheol. **62**, 643 (2018).
[30] F. Blanc, F. Peters, and E. Lemaire, Experimental signature of the pair-trajectories of rough spheres in the shear-induced microstructure in non-colloidal suspensions, Phys. Rev. Lett. **107**, 208302 (2011).
[31] H. Fahs, G. Ovarlez, and X. Chateau, Pair-particle trajectories in a shear flow of a bingham fluid, J. Non-Newt. Fluid Mech. **261**, 171 (2018).
[32] M. Firouznia, B. Metzger, G. Ovarlez, and S. Hormozi, The interaction of two spherical particles in simple-shear flows of yield stress fluids, J. Non-Newt. Fluid Mech. **255**, 19 (2018).
[33] G. Ovarlez, F. Mahaut, S. Deboeuf, N. Lenoir, S. Hormozi, and X. Chateau, Flows of suspensions of particles in yield stress fluids, J. Rheol. **59**, 1449 (2015).
[34] F. Blanc, F. Peters, and E. Lemaire, Local transient rheological behavior of concentrated suspensions, J. Rheol. **55**, 835 (2011).
[35] R. Lespiat, S. Cohen-Addad, and R. Höhler, Jamming and flow of random-close-packed spherical bubbles: an analogy with granular materials, Phys. Rev. Lett. **106**, 148302 (2011).
[36] L. Ducloué, O. Pitois, J. Goyon, X. Chateau, and G. Ovarlez, Rheological behaviour of suspensions of bubbles in yield stress fluids, J. Non-Newt. Fluid Mech. **215**, 31 (2015).
[37] I. Cantat, S. Cohen-Addad, F. Elias, F. Graner, R. Höhler, O. Pitois, F. Rouyer, and A. Saint-Jalmes, *Foams: structure and dynamics* (OUP Oxford, 2013).
[38] F. Mahaut, X. Chateau, P. Coussot, and G. Ovarlez, Yield stress and elastic modulus of suspensions of noncolloidal particles in yield stress fluids, J. Rheol. **52**, 287 (2008).
[39] X. Chateau, G. Ovarlez, and K. L. Trung, Homogenization approach to the behavior of suspensions of noncolloidal particles in yield stress fluids, J. Rheol. **52**, 489 (2008).
[40] G. Ovarlez, Q. Barral, and P. Coussot, Three-dimensional jamming and flows of soft glassy materials, Nature Mater. **9**, 115 (2010).
[41] G. Ovarlez, F. Bertrand, P. Coussot, and X. Chateau, Shear-induced sedimentation in yield stress fluids, J. Non-Newt. Fluid Mech. **177**, 19 (2012).
[42] J. Goyon, F. Bertrand, O. Pitois, and G. Ovarlez, Shear induced drainage in foamy yield-stress fluids, Phys. Rev. Lett. **104**, 128301 (2010).
[43] C. W. Macosko, *Rheology: principles, measurements, and applications* (Wiley-VCH, New York, 1994).
[44] A. Ramachandran and D. T. J. Leighton, Particle migration in concentrated suspensions undergoing squeeze flow, J. Rheol. **54**, 563 (2010).
[45] Q. Barral, *Superposition d'écoulements orthogonaux dans des fluides complexes : mise en place de l'expérience, application aux suspensions et aux fluides à seuil*, Ph.D. thesis, Université Paris-Est (2011).
[46] G. Ovarlez, Rheometry of visco-plastic fluids, in *Lectures on Visco-Plastic Fluid Mech.* (Springer, 2019) pp. 127–163.
[47] L. Feldkamp, L. Davis, and J. Kress, Practical cone-beam algorithm, JOSA A **1**, 612 (1984).
[48] The slight deviation from the circular symmetry of the unsheared bubble suspension (1) pdf in Fig. 5b – the circle for $\rho \simeq d$ appearing as a polygon – is observed too in the unsheared solid particle suspension (3), when particle center precision is limited to 1 voxel (without subvoxel identification).
[49] Figure 5b shows the average $g_r(\rho, \theta)$ over all θ for both solid particle (in red) and bubble (in black) suspensions, showing that the maximal value for bubbles is a bit lower (~ 1.2) than for solid particles (~ 1.5).
[50] J. R. Seth, L. Mohan, C. Locatelli-Champagne, M. Cloitre, and R. T. Bonnecaze, A micromechanical model to predict the flow of soft particle glasses, Nature Mater. **10**, 838 (2011).
[51] S. Karmakar, E. Lerner, and I. Procaccia, Plasticity-induced anisotropy in amorphous solids: The bauschinger effect, Phys. Rev. E **82**, 026104 (2010).
[52] S. Patinet, A. Barbot, M. Lerbinger, D. Vandembroucq, and L. Anaël, Origin of the bauschinger effect in amorphous solids, Phys. Rev. Lett. **124**, 205503 (2020).
[53] L. Ducloué, O. Pitois, J. Goyon, X. Chateau, and G. Ovarlez, Coupling of elasticity to capillarity in soft aerated materials, Soft Matter **10**, 5093 (2014).
[54] This exact value may depend on the spatial resolution chosen to compute the pdf g and its average (size of the elementary sampling volumes) and on the inclusion polydispersity [29]. In the following, the spatial resolution is kept constant, so that values of g from different samples

of solid suspensions are comparable to each other. As shown in Sec. II C 2, it is a bit lower for bubbles (~ 1.2) than for solid particles (~ 1.5), so over-population and depletion of bubbles can be identified, respectively, with $g_r > 1.2$ and $g_r < 1.2$.

[55] F. Peters, G. Ghigliotti, S. Gallier, F. Blanc, E. Lemaire, and L. Lobry, Rheology of non-brownian suspensions of rough frictional particles under shear reversal: A numerical study, J. Rheol. **60**, 715 (2016).

[56] F. Blanc, *Rhéologie et microstructure des suspensions concentrées non browniennes*, Ph.D. thesis, Université Nice Sophia Antipolis (2011).

[57] S. Gallier, E. Lemaire, F. Peters, and L. Lobry, Rheology of sheared suspensions of rough frictional particles, J. Fluid Mech. **757**, 514 (2014).

[58] D. Fraggedakis, Y. Dimakopoulos, and J. Tsamopoulos, Yielding the yield-stress analysis: a study focused on the effects of elasticity on the settling of a single spherical particle in simple yield-stress fluids, Soft Matter **12**, 5378 (2016).